2. Linear Theory[1]

2.1 Introduction

Here, a linear analytical model of the boundary layer flow in a translating tropical cyclone is presented and analysed. This model is an extension of the classical Ekman boundary layer model, and of earlier work on boundary layers in stationary vortices. It will be argued that such an Ekman-type model is appropriate in tropical cyclones since diurnal effects are weak or absent, turbulence is dominantly shear-generated, and baroclinicity is weak. The major assumptions necessary to achieve an analytical solution are a simplified form of the vertical diffusion, the omission of vertical advection, and linearisation of the horizontal advection, although relaxation of the second of these will be discussed. The solution is shown to have three components, a symmetric one due to the cyclone, and two asymmetric ones that result from the interaction of the moving cyclone with the earth's surface. The asymmetric components are shown to be equivalent to a frictionally stalled inertia wave, anchored in position by the asymmetric surface friction.

The jet in the upper part of the boundary layer is similar to the supergeostrophic flow found at the top of the classical Ekman spiral. It is only a few percent supergradient in the linear model, although it will be shown that the neglect of vertical advection substantially reduces the strength. The jet height scales as $(2K/I)^{1/2}$, where K is the turbulent diffusivity and I the inertial stability, modulated by a function of a dimensionless parameter. This height is typically several hundreds of metres in the cyclone core, and increases with radius. In a moving storm, the jet is most supergradient

[1]With the exception of section 2.5, most of the material in this chapter was published as Kepert (2001).

– several times stronger than in a stationary storm – at the eyewall to the left (right) and front of the storm in the Northern (Southern) Hemisphere. It also extends over a large area to the left (right) of the storm. It is, however, much less marked to the right (left), where the strongest near-surface winds are found.

Current operation practise is that the factor for reducing upper winds to a near-surface equivalent depends on the static stability and surface roughness only. This factor will be shown to have a substantial spatial variability, also. Larger values are found near the eye due to the symmetric component of the solution. There is also a marked overall increase from right to left (left to right) of the storm in the Northern (Southern) Hemisphere; that is, the surface wind reduction factor tends to be stronger on the side of the storm with weaker surface winds.

2.2 Derivation of the Linear Model

A linear analytical model for the boundary layer flow in a tropical cyclone is now developed. The formulation and solutions have some features in common with the well-known Ekman spiral model of the boundary layer, but with some important differences. The symmetric part, applicable to a stationary vortex, is similar to the model proposed by Eliassen and Lystad (1977, henceforth EL77), although they obtained numerical rather than analytical solutions. Their most intense vortex had a Rossby number of 20[2], which is below tropical cyclone strength. However, their model has been verified in more intense cyclones by Montgomery et al. (2001). The symmetric component was also considered by Rosenthal (1962), although with a less accurate linearisation of the surface boundary condition. The solution will be studied for a wider range of conditions than was done by these earlier investigators. A significant advance here is that the asymmetric components, which arise in a moving storm, do not appear to have been investigated before.

The horizontal momentum equations for a steady-state vortex with constant vertical turbulent diffusivity and no horizontal diffusion, in cylindrical coordinates moving with the vortex, on an *f*-plane, are

$$\begin{aligned} u\frac{\partial u}{\partial r} + \frac{v}{r}\frac{\partial u}{\partial \lambda} + w\frac{\partial u}{\partial z} - \left(f + \frac{v}{r}\right) v &= -\frac{\partial \varphi}{\partial r} + K\frac{\partial^2 u}{\partial z^2} \\ u\frac{\partial v}{\partial r} + \frac{v}{r}\frac{\partial v}{\partial \lambda} + w\frac{\partial v}{\partial z} + \left(f + \frac{v}{r}\right) u &= K\frac{\partial^2 v}{\partial z^2} \end{aligned} \qquad \textbf{(2.1)}$$

[2]Eliassen and Lystad (1977) used a vortex given in dimensional terms by $V(r) = r\ \mathrm{Ro}\ f/(2(1 + (r/r_m)^2))$ where r_m the radius of maximum winds, and f the Coriolis parameter. Thus the Rossby number is $\mathrm{Ro} = 4v_m/(fr_m)$, where v_m is the maximum wind,.

The symmetric gradient-level flow, V, is assumed to be in balance with the pressure gradient, $fV + V^2/r = \partial\varphi/\partial r$. Additionally, the vortex is assumed to move with the environmental flow, U_t, which is in geostrophic balance. When subtracting off the vortex motion to obtain (2.1), the corresponding environmental geostrophic pressure gradient was also removed, so there is no $\partial\varphi/\partial\lambda$ term. Equation (2.1) is linearised by replacing v by $V + v$, assuming $u, v, w << V$ and neglecting terms of second and higher order in u, v and w to give

$$\begin{aligned} \frac{V}{r}\frac{\partial u}{\partial \lambda} - v\left(f + \frac{2V}{r}\right) &= K\frac{\partial^2 u}{\partial z^2} \\ \frac{V}{r}\frac{\partial v}{\partial \lambda} + u\left(f + \frac{V}{r} + \frac{\partial V}{\partial r}\right) &= K\frac{\partial^2 v}{\partial z^2}. \end{aligned} \qquad \textbf{(2.2)}$$

Here, it has been additionally assumed that the base state vortex is symmetric and barotropic, $V = V(r)$. In the limit $r \to \infty$, (2.2) reduces to the classic Ekman equations in Cartesian coordinates.

Equations (2.2) represent the radial flow balance between accelerations due to azimuthal advection, gradient-wind imbalance, and turbulent transport, and the balance for the azimuthal component, between the azimuthal and radial advection of absolute angular momentum, and its turbulent transport, respectively. This linearization will not be valid in the case of an inertially neutral storm, when the coefficient of u in the second of (2.2) will become 0, and other processes will have to balance the turbulent transport of v. This case will be explored in chapter 3. Note that Smith (1968) commented that the removal of vertical advection is not supported by scale analysis. In particular, for a symmetric vortex within the radius of maximum inflow, the continuity equation gives $W/H \sim V/R$, where W and V are scales for vertical and horizontal velocity, and H and R are vertical and horizontal length scales. Then the vertical advection terms in (2.1) scale

as $WV/H \sim V^2/R$, which is the same order as other terms retained in (2.2). This will later be shown to be one of the major sources of differing predictions by this linear model, and the numerical model to come. However, the linear model will be seen to contain useful physical insight, even though the neglect of vertical advection is not strictly justified.

Equations (2.2) may be written as

$$2\gamma \frac{\partial \omega}{\partial \lambda} + 2i\sqrt{\alpha\beta}\ \omega - \frac{\partial^2 \omega}{\partial z^2} = 0 \qquad \textbf{(2.3)}$$

where u and v have been combined into the complex variable

$$\omega = \sqrt{\frac{\beta}{\alpha}}\ u + iv \qquad \textbf{(2.4)}$$

and

$$\begin{aligned} \alpha &= \frac{1}{2K}\left(f + \frac{2V}{r}\right) \\ \beta &= \frac{1}{2K}\left(f + \frac{V}{r} + \frac{\partial V}{\partial r}\right) \\ \gamma &= \frac{1}{2K}\frac{V}{r} \end{aligned} \qquad \textbf{(2.5)}$$

Expanding (2.3) as a Fourier series in azimuth gives

$$\omega(\lambda, z) = \sum_{k=-\infty}^{\infty} a_k(z)\ e^{ik\lambda} \qquad \textbf{(2.6)}$$

for complex coefficients $a_k(z)$, whence

$$\sum_{k=-\infty}^{\infty} \left(2i \left(\gamma k + \sqrt{\alpha\beta} \right) a_k(z) - a_k''(z) \right) e^{ik\lambda} = 0 \qquad \textbf{(2.7)}$$

Equating coefficients of $\exp(ik\lambda)$ to zero gives a family of second order ordinary differential equations in $a_k(z)$. Seeking solutions $a_k(z) = A_k \exp(p_k z)$ for some constants A_k and p_k, yields

$$p_k = \pm(1 + i) \sqrt{\sqrt{\alpha\beta} + k\gamma}. \qquad \textbf{(2.8)}$$

The solution with positive real part is immediately eliminated because of the boundary condition that the perturbations u and v go to zero as $z \to \infty$. The required root will be written as

$$p_k = \begin{cases} -(1 + i) \sqrt{\sqrt{\alpha\beta} + k\gamma}, & \sqrt{\alpha\beta} + k\gamma > 0 \\ -(1 - i) \sqrt{|k|\gamma - \sqrt{\alpha\beta}}, & \sqrt{\alpha\beta} + k\gamma < 0. \end{cases} \qquad \textbf{(2.9)}$$

To avoid the potential confusion of deciding which complex square root to take, expressions will always be written so only positive real numbers appear under the square root sign. While the former case will prevail in the cyclone core for low wave numbers $|k|$, the latter can occur anywhere for sufficiently large negative k but may occur outside the core even for $k = -1$, in storms with a moderately peaked radial wind profile and hence weak relative vorticity. The implications of this change of sign will be discussed further below. In the intermediate case $(\alpha\beta)^{1/2} + k\gamma = 0$, both roots are zero.

The usual approach to solving the Ekman equations uses a no-slip lower boundary condition, $u(0) = 0$, $v(0) = -V$. This does not well represent atmospheric conditions and also grossly violates the linearization here. Instead, a slip condition is

applied near the surface, using a bulk formulation with drag coefficient C for the near-surface stress after Taylor (1916),

$$K \frac{\partial u}{\partial z} = C \sqrt{(u+u_t)^2 + (V+v+v_t)^2}\ (u+u_t)$$
$$K \frac{\partial v}{\partial z} = C \sqrt{(u+u_t)^2 + (V+v+v_t)^2}\ (V+v+v_t). \qquad \textbf{(2.10)}$$

This is evaluated at some height in the surface layer, which for convenience is taken to be $z = 0$. Here, (u_t, v_t) is the cyclone translation velocity, which is taken as being in the positive x direction with speed U_t, giving

$$u_t = \frac{1}{2} U_t \left(e^{i\lambda} + e^{-i\lambda}\right)$$
$$v_t = \frac{i}{2} U_t \left(e^{i\lambda} - e^{-i\lambda}\right) \qquad \textbf{(2.11)}$$

Assuming that $U_t << V$, (2.10) may be linearised to

$$C\ V \left(u(0) + u_t \right) = K \left.\frac{\partial u}{\partial z}\right|_{z=0}$$
$$C\ V \left(V + 2v(0) + 2v_t \right) = K \left.\frac{\partial v}{\partial z}\right|_{z=0} \qquad \textbf{(2.12)}$$

This assumption implies that the model is applicable only in the core region, or for very slowly moving cyclones. Equations (2.12) cannot be written as an algebraic function of ω, so it is necessary to separate out the real and imaginary parts of (2.6), giving

$$\mathrm{Re}\left[\sqrt{\frac{\alpha}{\beta}} \sum_{k=-\infty}^{\infty} A_k \left(\frac{CV}{K} + (1+i)\sqrt{\sqrt{\alpha\beta} + k\gamma} \right) e^{ik\lambda} + \frac{1}{2}\frac{CV}{K} U_t \left(e^{i\lambda} + e^{-i\lambda} \right) \right] = 0$$

$$\mathrm{Im}\left[\sum_{k=-\infty}^{\infty} A_k \left(\frac{2CV}{K} + (1+i)\sqrt{\sqrt{\alpha\beta} + k\gamma} \right) e^{ik\lambda} + \frac{CV}{K} \left(U_t \left(-e^{i\lambda} + e^{-i\lambda} \right) + iV \right) \right] = 0 \qquad \textbf{(2.13)}$$

A little care is needed in solving (2.13). Having taken real and imaginary parts, it is not correct to simply equate coefficients of powers of exp($ik\lambda$) to 0. One route is to substitute in some suitable values for λ and solve the resulting system of equations. A more elegant approach is to use the identities Re(z) = (z + z*)/2, Im(z) = i(-z + z*)/2, where z* is the complex conjugate of z, to eliminate the Re and Im functions. The coefficients of exp($ik\lambda$) in the pair of equations thus obtained from (2.13) must then be 0. This gives a system of linear equations in A_k and A_k*, which are straightforward to solve. For $|k| \geq 2$, $A_k = 0$, since in a linear model with the present surface boundary condition there is nothing to excite wave numbers above one. For $|k| \leq 1$ and $(\alpha\beta)^{1/2} - \gamma > 0$,

$$A_1 = -\frac{\eta \left[1 - 2\sqrt{\alpha/\beta} + (1+i)(1-\sqrt{\alpha/\beta})\psi \right] U_t}{\sqrt{\alpha/\beta} \left[(2+2i)(1+\eta\psi) + 3\eta + 3i\psi \right]}$$

$$A_0 = -\frac{\chi \left[1 + i(1+\chi) \right] V}{2\chi^2 + 3\chi + 2} \qquad \textbf{(2.14)}$$

$$A_{-1} = -\frac{\psi \left[1 + 2\sqrt{\alpha/\beta} + (1+i)(1+\sqrt{\alpha/\beta})\eta \right] U_t}{\sqrt{\alpha/\beta} \left[(2+2i)(1+\eta\psi) + 3\psi + 3i\eta \right]}$$

where

$$\eta = \frac{CV}{K\sqrt{\sqrt{\alpha\beta} + \gamma}} = CV\sqrt{\frac{2}{K\,(V/r + I)}}$$

$$\chi = \frac{CV}{K\,(\alpha\beta)^{1/4}} = CV\sqrt{\frac{2}{K\,I}} \qquad \textbf{(2.15)}$$

$$\psi = \frac{CV}{K\sqrt{\left|\sqrt{\alpha\beta} - \gamma\right|}} = CV\sqrt{\frac{2}{K\left|V/r - I\right|}}$$

are dimensionless numbers, and $I^2 = (f + 2V/r)(f + V/r + \partial V/\partial r)$ is the square of the inertial stability. For $(\alpha\beta)^{1/2} - \gamma < 0$ (or equivalently, $I < V/r$), a slightly different form is obtained for the asymmetric components[3]

$$A_1' = -\frac{\eta\,[\,1 - 2\sqrt{\alpha/\beta} + (1 - i)(1 - \sqrt{\alpha/\beta})\,\psi\,]\,U_t}{\sqrt{\alpha/\beta}\,[\,2 + 2i + 3\,(\eta + \psi) + (2 - 2i)\,\eta\psi\,]}$$

$$A_{-1}' = -\frac{\psi\,[\,1 + 2\sqrt{\alpha/\beta} + (1 + i)(1 + \sqrt{\alpha/\beta})\,\eta\,]\,U_t}{\sqrt{\alpha/\beta}\,[\,2 - 2i + 3\,(\eta + \psi) + (2 + 2i)\,\eta\psi\,]} \qquad \textbf{(2.16)}$$

using A' instead of A to avoid ambiguity.

The boundary layer flow is thus given by

$$u(\lambda,z) = u_1(\lambda,z) + u_0(z) + u_{-1}(\lambda,z)$$
$$v(\lambda,z) = v_1(\lambda,z) + v_0(z) + v_{-1}(\lambda,z) \qquad \textbf{(2.17)}$$

where u_0 and v_0 are respectively $(\alpha/\beta)^{1/2} = ((f + 2V/r) / (f + V/r + \partial V/\partial r))^{1/2}$ times the real

[3] If ψ is replaced by $-i\psi$ for A_1 and by $i\psi$ for A_{-1} in (2.16), then (2.14) is obtained.

part, and the imaginary part, of

$$\omega_0(z) = A_0 \exp\left(- \frac{(1 + i)\, z}{\delta_0} \right) \qquad \textbf{(2.18)}$$

The asymmetric components (u_1, v_1) and (u_{-1}, v_{-1}) are similarly obtained from

$$\omega_1(\lambda, z) = \begin{cases} A_1 \exp\left(- \dfrac{(1 + i)z}{\delta_1} + i\lambda \right), & I > V/r \\ A_1' \exp\left(- \dfrac{(1 + i)z}{\delta_1} + i\lambda \right), & I < V/r \end{cases} \qquad \textbf{(2.19)}$$

and

$$\omega_{-1}(\lambda, z) = \begin{cases} A_{-1} \exp\left(- \dfrac{(1 + i)z}{\delta_{-1}} - i\lambda \right), & I > V/r \\ A_{-1}' \exp\left(- \dfrac{(1 - i)z}{\delta_{-1}} - i\lambda \right), & I < V/r \end{cases} \qquad \textbf{(2.20)}$$

The depth scales of the three components are

$$\delta_k = \frac{1}{\sqrt{\left| \sqrt{\alpha\beta} + k\gamma \right|}} = \sqrt{\frac{2K}{\left| I + kV/r \right|}} \qquad \textbf{(2.21)}$$

The solutions (2.19) are continuous at those radii where $I = V/r$, if such exist, although the radial gradients become large. The behaviour there will be discussed further below.

The frictionally-induced agradient flow has thus been decomposed into three components. The two components with azimuthal wave-number one are proportional to product of the translation speed U_t and the gradient wind speed V, while the

symmetric component is proportional to V^2. Each solution has a different depth scale δ_k, which is greatest for $k = -1$, and least for $k = 1$. A physical explanation for these different length scales is given later. Note that because of the linearization of the surface boundary condition in (2.12), and particularly the assumption $U_t << V$, the asymmetric parts of the solution do not reduce to the Ekman limit for straight flow far from the vortex, although the symmetric part does. In fact, as $r \to \infty$, each of A_0/V^2, $A_1/(VU_t)$ and $A_{-1}/(VU_t)$ approach nonzero constants, so each of the $(u_k, v_k) \to 0$. However, in the absence of that linearisation, the asymmetric components would become proportional to U_t^2 in that limit, and so are valid only in that part of the vortex where $V >> U_t$. Note also that the limiting behaviour $A_0 \sim V^2$ for small V follows from the semi-slip boundary condition, rather than the circular geometry. Exactly the same behaviour arises when the classical Ekman equations in Cartesian coordinates are solved with this boundary condition.

The symmetric and asymmetric components of the solution are now considered separately.

2.3 The boundary layer of a stationary vortex

2.3.1 Horizontal Flow

Here, only the symmetric part (u_0, v_0) of the solution applies. It differs from the classical Ekman spiral in three ways. The first is that the depth scale is $\delta_0 = (2K/I)^{1/2}$, which in the core of a tropical cyclone is much less than $\delta_E = (2K/f)^{1/2}$. The effect of storm rotation in reducing the depth of the boundary layer has been noted before, for example by EL77, Anthes and Chang (1978) and Frank (1984), the latter two of whom took the depth as being proportional to $(f + 2V/r)^{-1/2}$. The analysis here, which will be confirmed by the numerical modelling results in Chapter 3, suggests that $(2K/I)^{1/2}$ is a more appropriate scale.

The second important difference is that the square root term in (2.4) alters the degree of turning of wind direction with height from the classic solution. Inside the eye of a cyclone, this term will be close to 1. However, outside the eye, V/r and $\partial V/\partial r$ have opposite signs and will partially cancel, leading to a stronger cross-isobaric component, relative to the along-isobaric component, than in the solution for straight flow. This will become more marked as the inertial stability of the storm decreases towards neutrality, until at the neutral limit (where the model ceases to be valid) $\beta = 0$. Further, the change in sign of $\partial V/\partial r$ at the radius of maximum winds will produce a marked radial gradient in the near-surface inflow there, and hence substantial near-surface convergence. The vertical velocity forcing implied by this solution will be discussed in detail below.

The final important difference lies in the coefficient A_0, which affects the phase and amplitude of the spiral. This is different because of both the slip boundary condition, and the arbitrary definition of $z = 0$ as being some height in the surface layer, rather than the actual surface. While the first two of the differences noted here are due to the

application to a vortex, this latter one is rather a consequence of the surface boundary condition. Indeed, the solution for horizontally homogeneous geostrophically balanced straight flow in Cartesian coordinates with this surface boundary condition may be recovered from (2.18) by replacing I by f in the definition (2.15) of χ ,and setting the coefficient $(\alpha/\beta)^{1/2}$ used in extracting u from (2.18) equal to 1.

The variation of the dimensionless parameter χ with wind speed is clearly of interest. Unfortunately, determining this is not easy, as C, K and I will each vary with V. Of these, the turbulent diffusivity is perhaps the most difficult dependence to assign. One possibility is to take the turbulence length scale as proportional to height, on the grounds that the turbulence is predominantly shear generated. Thus a representative length scale for the whole boundary layer, as required here, is the boundary layer depth δ_0, and the diffusivity can be parameterised as

$$K \sim (\text{turbulent length scale})^2 \left| \text{shear} \right| \sim \delta_0^2 \frac{V}{\delta_0} = \delta_0 V \qquad \textbf{(2.22)}$$

Substituting this and the definition of δ_0 into the second of (2.15) gives $\chi \sim C$. The approximately linear increase of C with wind speed, at least up to 25 m s^{-1}, is well documented (e.g. Garrett 1977, Large and Pond 1981), although there is some disagreement about whether this increase is maintained at higher speeds (e.g. Frank 1984, Hubbert et al. 1991). Using (2.21) in (2.22) gives $K \sim V^2/I$ and hence

$$\delta_0 \sim \frac{V}{I} \qquad \textbf{(2.23)}$$

removing the dependence on turbulence parameters. This result, while potentially useful,

relies on a scaling argument for the turbulence parameters, and so should be used with caution. This point is revisited in Chapter 3.

The height of the maximum azimuthal wind and the wind components there may be found by solving $\partial v_0/\partial z = 0$, giving

$$
\begin{aligned}
z_{\max} &= \delta_0 \arctan(-1 - 2/\chi) \\
u_0(z_{\max}) &= -V \frac{e^{-\arctan(-1 - 2/\chi)}}{\sqrt{2}} \frac{\chi\sqrt{\chi^2 + 2\chi + 2}}{2\chi^2 + 3\chi + 2} \sqrt{\frac{\alpha}{\beta}} \\
v_0(z_{\max}) &= V \frac{e^{-\arctan(-1 - 2/\chi)}}{\sqrt{2}} \frac{\chi\sqrt{\chi^2 + 2\chi + 2}}{2\chi^2 + 3\chi + 2}
\end{aligned}
\qquad \textbf{(2.24)}
$$

Values for the arctan function here lie in the range $\pi/2$ to $3\pi/4$, so the precise details of the storm can vary the height of the jet by about 50% within our scale estimate of δ_0. That $u_0(z_{max}) < 0$ is important for two reasons: physically because it shows that there is inflow in the presence of supergradient azimuthal flow, and mathematically since it shows that $v_0(z_{max})$ is indeed a maximum, as $\partial^2 v_0/\partial z^2(z_{max}) = 2\beta u_0(z_{max}) < 0$. Note here that an inertially more neutral storm will have a higher jet, through both δ_0 and the arctan term, and that increasing the drag coefficient will lower the jet. Further, the strength of the jet relative to the gradient flow is expressed entirely in terms of χ. Figure 2.1 shows the effect of individually varying the five of six parameters (diffusivity, drag coefficient, gradient wind speed, radius and inertial stability – the effect of varying latitude is, unsurprisingly, negligible) through a physically reasonable range, on jet height and relative strength. Here the inertial stability is parameterised through a variable x, defined by $\partial V/\partial r = xV/r$, and the parameters are varied about the values $K = 50$ m^2 s^{-1}, $C = 0.002$, $V = 40$ m s^{-1}, $f = 3.77\times10^{-5}$ s^{-1} (for latitude 15°), $r = 40$ km, and $x = -0.5$ (Gray and Shea 1973).

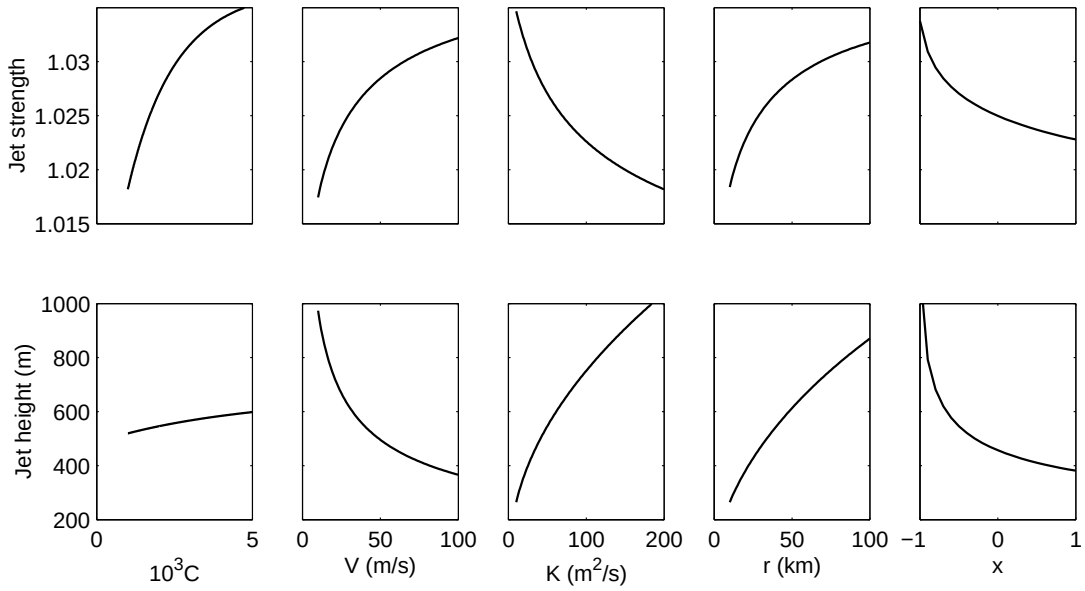

Figure 2.1: The variation of relative jet strength (top) and jet height (bottom) with various parameters in the linear model, according to (2.24). For each pair of graphs, the parameters not varying have values $C = 0.002$, $V = 40$ m s^{-1}, $K = 50$ m^2 s^{-1}, $r = 40$ km and $x = -0.5$.

The jet in this linear model is typically from 2% to 4% supergradient and thus substantially weaker than in the observations. It will be argued later in this chapter, and confirmed in the next, that this is a consequence of the linear model, and that incorporating the vertical advection produces a result more consistent with the observations.

An interesting feature of Fig 2.1 is that increasing the drag coefficient (over the range given) markedly increases the jet strength, with only a minor effect on the height. This is because greater surface friction leads to stronger inflow through much of the boundary layer, and hence greater inwards advection of angular momentum. This is potentially important, because of both the poorly known wind speed dependence of the drag coefficient at high winds, and the marked increase that (usually) occurs at landfall. The time scale for the boundary layer to develop was shown by EL77 to be $1/I$, and is less than an hour for the inner part of a hurricane. This therefore suggests that the jet may strengthen as strong winds cross the coast.

Increasing the gradient wind speed on its own is seen to lead to a shallower, stronger jet. However, note that in the real atmosphere stronger winds would be expected to lead also to an increase in turbulent diffusivity and drag coefficient. The increase in K would tend to reverse this trend, while the increase in C would further increase the strength, but slightly increase the height.

Varying the radius alters the inertial stability, leading to a lower but weaker jet for a more compact storm, all other things being equal. Finally, the effect of varying the radial profile of the gradient wind is that, in a more peaked, inertially neutral storm, x will be closer to -1, giving a stronger but higher jet. Note also that just inside the radius

of maximum winds, where x is positive, the jet is predicted to be lower and weaker than just outside. However, care is needed in interpreting this last pair of panels for in-eye conditions as the gradient wind speed is held constant for them.

2.3.2 Vertical velocity forcing in a stationary vortex

The vertical velocity above the boundary layer can be found by integrating the continuity equation vertically and applying the surface boundary condition $w = 0$, giving

$$\begin{aligned} w_\infty(r) &= -\frac{1}{r}\frac{\partial}{\partial r}\left(r \int_0^\infty u \, dz \right) \\ &= \frac{1}{r}\frac{\partial}{\partial r}\left(\frac{r\, C\, V\, (V + 2v(0))}{f + V/r + \partial V/\partial r} \right) \end{aligned} \qquad \textbf{(2.25)}$$

Here, (2.2) and (2.12) were used to write

$$\begin{aligned} \int_0^\infty u(z)\, dz &= \frac{\int_0^\infty v''(z)\, dz}{K(f + V/r + \partial V/\partial r)} = \frac{v'(\infty) - v'(0)}{K(f + V/r + \partial V/\partial r)} \\ &= -\frac{CV(V + 2v(0))}{f + V/r + \partial V/\partial r} \end{aligned} \qquad \textbf{(2.26)}$$

in a stationary vortex. A similar result was found by EL77. This has several interesting consequences. Firstly, it is nearly independent of K – only the weak influence through $v(0)$ remains. Secondly, if the radial variation of $(f + V/r + \partial V/\partial r)^{-1}$ in (2.25) can be neglected, it is clear that the Ekman pumping velocity is proportional to the curl of the surface stress, as in the classical solution. However, neglecting this gradient is clearly invalid near the eyewall, and also where the vorticity is small. Finally, assuming for the moment that $v(0)$ is proportional to V, it is easy to consider three particular cases:

- Solid body rotation $V = \Omega r$, and w_∞ is proportional to r; that is, frictional forcing produces ascent proportional to radius in the eye. This result was also obtained

by Eliassen (1971) and EL77.

- Rankine vortex $dV/dr = -V/r$, and w_∞ is proportional to $-1/r^3$ giving subsidence increasing rapidly towards the centre of the storm. Thus storms with a highly peaked wind profile will be subsident outside the radius of maximum winds (RMW), although note that this case approaches the limits of applicability of the linear model. The subsidence here is quite different to the predictions of the standard Ekman model for this case, which predicts zero vertical velocity from the irrotational gradient level flow. However, Carrier (1971, see correction in a footnote due to J. McWilliams) found subsidence proportional to r^{-2} in a similar vortex. The weaker radial dependence found by them is due to their use of a no-slip surface boundary condition.
- Typical cyclone with V proportional to r^{-x} and $x \approx 1/2$, and also $\partial V/\partial r + V/r >> f$. This gives w_∞ proportional to r^{-x} and hence to V, and upwards.

Comparing the latter two of these cases with the first confirms that the maximum updraft must lie in the vicinity of the RMW. Determining the precise location is somewhat more difficult and the major influences on it are discussed in section 2.3.5.

2.3.3 Surface wind reduction

Consider for simplicity the ratio of surface azimuthal wind component (rather than full surface wind speed) to gradient wind. This is substantially different only in the nearly inertially neutrality case, when the model is at the limits of its validity anyway. Then the surface wind factor (SWF) is

$$\frac{V + v(0)}{V} = \frac{\chi^2 + 2\chi + 2}{2\chi^2 + 3\chi + 2} \qquad \textbf{(2.27)}$$

which decreases monotonically from 1 at $\chi = 0$ to a limiting value of 1/2 as $\chi \to \infty$.

Reasonable values of the parameters (near the eyewall, $C = 0.002$, $V = 40$ m s^{-1}, $K = 50$ m^2 s^{-1}, and $I = 10^{-3}$ s^{-1}) give a factor of 0.81, which is consistent with the studies cited earlier. At larger radii, where χ is smaller, relatively weaker surface winds will be found. The observational studies cited earlier have shown that there is no universal constant surface wind factor, and have tended to ascribe the differences to stability effects. Here, it has been shown that dynamical factors play a substantial role.

2.3.4 Application to a typical cyclone

The above may readily be applied to any of the several analytical wind profiles in the literature. That of Holland (1980) is adopted, since it is in a form which enables easy adjustment of the storm intensity, maximum wind radius, and shape of the wind profile outside the radius of maximum winds, and it satisfies known constraints on radial variation of angular momentum. In addition, it has been widely used and received considerable verification against observations, both in the original paper and subsequently (e.g. Harper et al. 1989, 1993). The profile within the eye is slightly modified to remove the barotropic instability present there. This is not strictly necessary here, but will be in the next next chapter, and so is adopted here for consistency. The full details are deferred until then.

Figure 2.2a shows the radial profiles of gradient wind from the Holland profile, and "surface" wind speed components from the linear model here, for a cyclone with maximum wind speed 40 m s^{-1} at a radius of 40 km. The Holland *b* parameter, which controls the radial velocity gradient and hence the inertial stability outside the radius of maximum winds, is 1.3, which is an average value for tropical cyclones. The inflow is seen to increase inwards more slowly than the azimuthal wind, before decreasing again inside the radius of maximum winds. The surface azimuthal wind is about 77% of the

gradient wind outside the RMW, but relatively much stronger at and inside of the RMW (Fig. 2.2e). This follows from (2.27) and the radial variation of χ, which is nearly constant outside the RMW, where V and $I^{1/2}$ have similar radial tendencies, but decreases rapidly to 0 at the centre, as V decreases and $I^{1/2}$ remains large. The predicted near-surface azimuthal flow is very similar to the analysis of Mitsuta et al. (1988), shown here in Fig 1.8.

The jet strength (Fig. 2.2c) is quite weak, about 3% supergradient, outside the RMW, decreasing rapidly inside the eye, while its height (Fig 2.2d) decreases nearly linearly towards the centre. The vertical velocity at three levels is shown in Fig 2.2b; the peak at the RMW and approximately linear dependence inside are apparent, as predicted in the discussion above. An exact linear dependence is not found because the gradient wind profile used does not have a linear dependence on radius here. It is interesting that the radial profiles of w at 200 m and 500 m are much more peaked than the one for the limit as $z \to \infty$, and that the updraft slopes outwards with height. This is partly a reflection of the shallower boundary layer towards the centre, but also that the radius of maximum inflow tilts outwards with height. In fact, as was pointed out by Rosenthal (1962), the radius of maximum horizontal convergence lies just within the RMW at the surface. Further aloft, the maximum horizontal convergence moves further out, to approximately a radius of 150 km at a height of 1500 m in this case. The lower boundary layer flow at large radii is accelerating inwards, and so there is comparatively weak low-level convergence there.

Figure 2.2f shows the diffusive forcing of inflow $K \partial^2 u/\partial z^2$ at the jet height. In the present model, this is all that balances the outwards acceleration due to gradient wind imbalance. In the real atmosphere, inflow is additionally forced by vertical advection

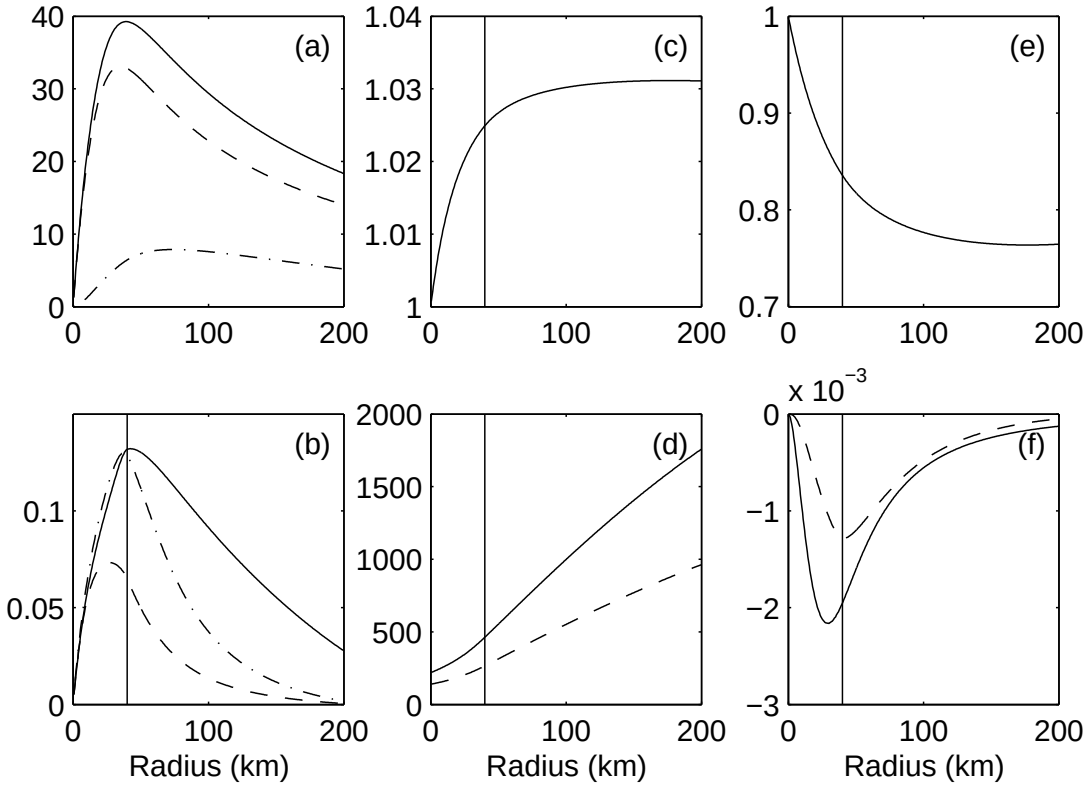

Figure 2.2: Radial profiles of (a) gradient wind (solid), surface azimuthal (dashed) and inflow (dash-dotted) components; (b) vertical velocity at 200 m (dashed), 500 m (dash-dot) and infinity (solid); (c) jet strength relative to the gradient wind; (d) jet height (solid) and depth scale δ_0 (dashed); (e) surface wind reduction factor and (f) forcing of inflow at the jet height by vertical diffusion (solid) and vertical advection (dashed). The cyclone is prescribed by the analytic model of Holland (1980) with r_{max} = 40 km, V_{max} = 40 m s^{-1}, and b = 1.3, with the eye modification described in the next chapter. Other parameters are C = 0.002, K = 50 m^2 s^{-1}, latitude 15°N.

$-w\,\partial u/\partial z$, which is shown dashed in Fig 2.2f, using w calculated from the modelled horizontal wind field by integrating the continuity equation. This is comparable to the diffusive forcing of inflow, and had it been included in the model, a more strongly supergradient flow could have been maintained in the upper boundary layer. Thus the present model underestimates the jet strength in the core region. Note that this argument is indicative rather than quantitative, as the vertical velocity field would be different in a nonlinear model. Inclusion of a crude representation of vertical advection will be considered in section 2.5, and it and the other nonlinear terms are considered in detail in Chapter 3.

2.3.5 The location of the maximum updraft

Eliassen and Lystad (1977) found in their numerical results that the maximum updraft was always located within the radius of maximum winds of their vortex, and that it moved outwards as the vortex became stronger, and inwards as the drag coefficient increased. However, when the updraft for the parametric wind profile of Holland (1980) was calculated, the location of the maximum updraft above the boundary layer fell slightly outside of the radius of maximum winds. Here, the analytical model is used to explain the sensitivity of updraft location to vortex strength and drag coefficient noted by EL77, and show that the maximum updraft for storms stronger than they considered lies outside the radius of maximum winds, in this model.

Using (2.27) in (2.25) gives

$$w_\infty(r) = \frac{\chi+2}{2\chi^2+3\chi+2}\,\frac{1}{r}\,\frac{\partial}{\partial r}\left(\frac{rCV^2}{f+V/r+\partial V/\partial r}\right) - \frac{2(\chi^2+4\chi+2)}{(2\chi^2+3\chi+2)^2}\,\frac{\partial\chi}{\partial r}\,\frac{CV^2}{f+V/r+\partial V/\partial r} \qquad \textbf{(2.28)}$$

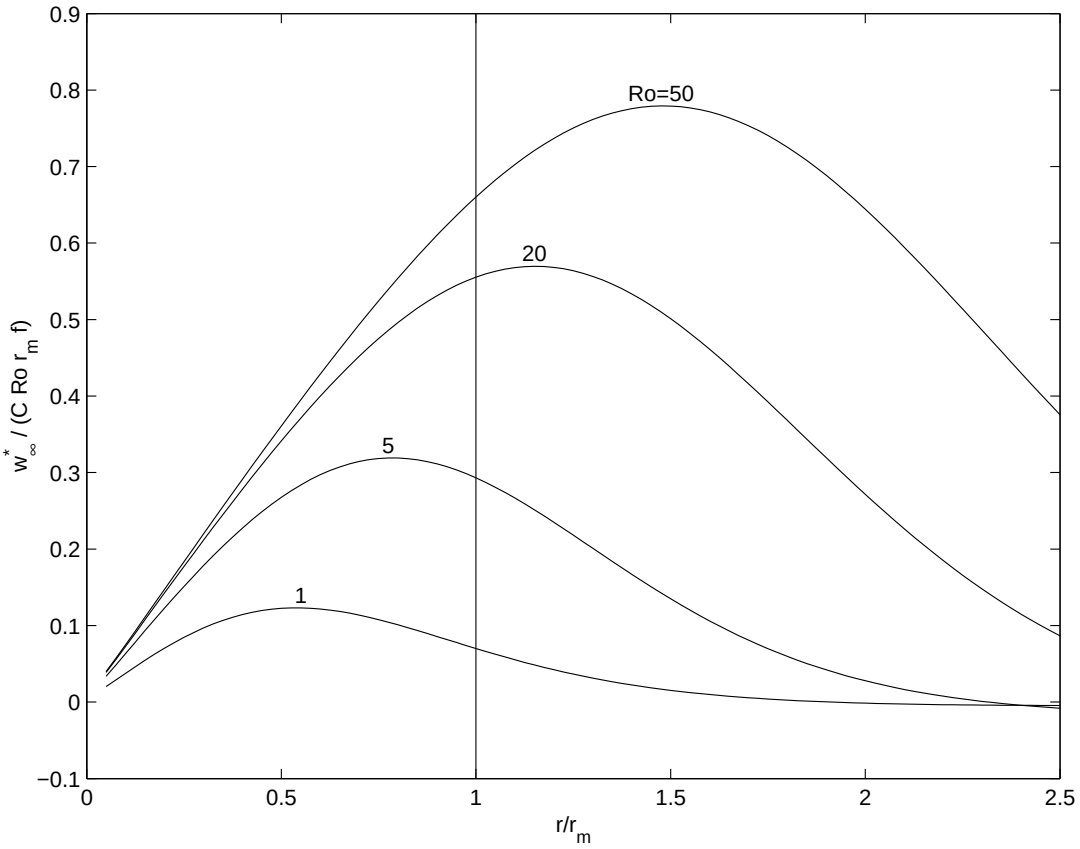

Figure 2.3: The approximate updraft w_∞^* in the limit $C \to 0$, for various Ro (as marked) in the vortex of EL77. The position of the maximum updraft moves outwards with increasing Ro, due to the change in relative importance of the planetary and relative vorticities in the denominator of (2.29).

EL77's vortex is given in dimensional form by $V = r\,\mathrm{Ro}\,f / (2(1 + (r/r_m)^2))$, where Ro is the Rossby number and r_m the radius of maximum winds. Ignoring for the moment the radial variation of χ, the updraft is approximately proportional to

$$w_\infty^*(r) = \frac{1}{r}\frac{\partial}{\partial r}\frac{rCV^2}{f + V/r + \partial V/\partial r} = \frac{C\mathrm{Ro}^2 f}{r}\frac{\partial}{\partial r}\frac{r^3}{\mathrm{Ro} + (1 + (r/r_m)^2)^2} \qquad \textbf{(2.29)}$$

Clearly, the shape of this curve as a function of r/r_m depends only upon Ro, and varying the other parameters will change only the magnitude. It is plotted for four different values of Ro in Fig 2.3, including EL77's maximum of Ro = 20; the outwards displacement of the maximum for more intense vortices is clear.

This placement of the maximum updraft outside of the RMW is in disagreement with observations, which place it immediately inside the RMW. This is partly because the limit w_∞ is being considered here, and the updraft slopes outward with height, as shown in Fig 2.2b. It may also be a consequence of the neglect in the linear model of some terms in the radial momentum budget equation which might be expected to be important near the RMW; in particular the vertical and radial advection.

Figure 2.4 shows w_∞ from (2.28) for the parametric vortex of EL77 with Ro = 20 and various C. As C increases, the maximum updraft moves inwards and broadens, with w_∞ being constant through much of the eye for $C = 0.02$. Note that the curves in Figs 2.3 and 2.4 are not exactly the same as in EL77, since

(i) in Fig 2.3 they are effectively the limit as $C \to 0$,

(ii) EL77 considered a slowly decaying vortex after the boundary layer was spun up, while these results are for a steady-state vortex,

(iii) EL77 had an upper boundary at height $4.9\delta_0$, and

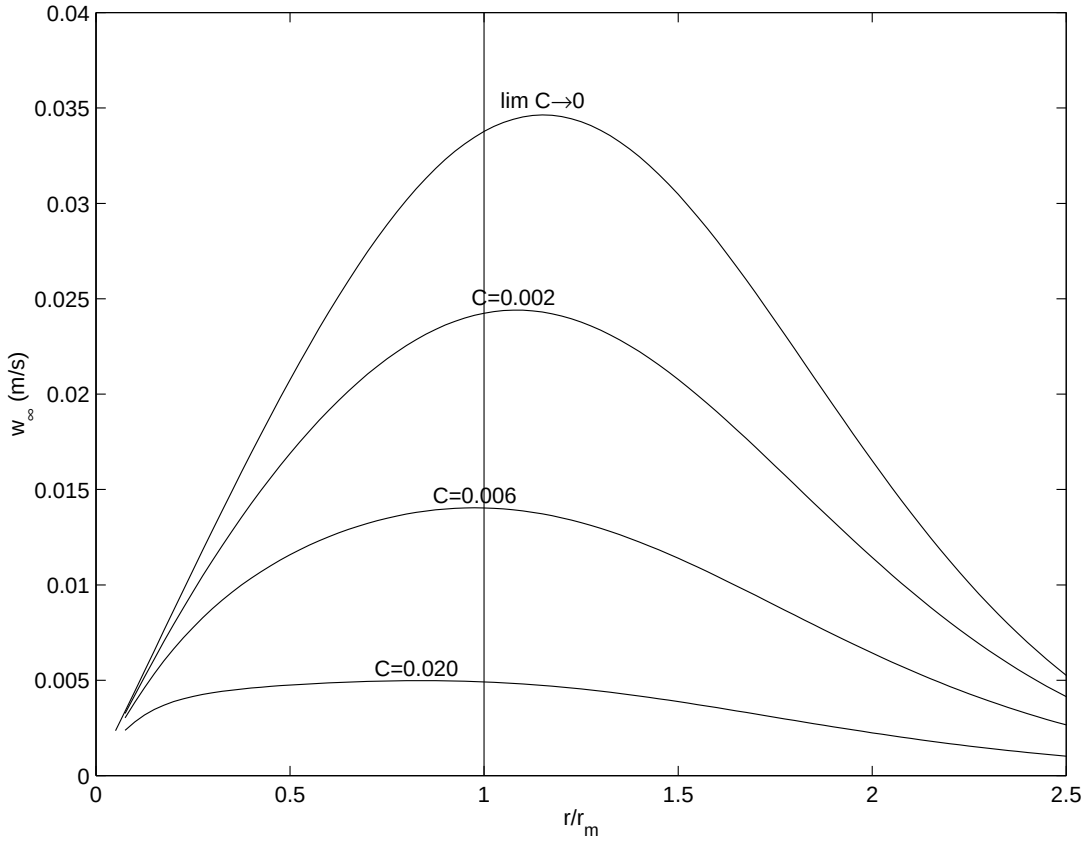

Figure 2.4: The updraft w_∞ for the vortex of EL77 for Ro = 20 and C = 0.002, 0.006, 0.02, and the approximate updraft w_∞'/C, labelled lim$C \to 0$. The parameter χ at the RMW is 0.27, 0.82, and 2.74 respectively, for the curves with nonzero C.

(iv) EL77's results were at the level of maximum updraft, while here they are as $z \to \infty$, and the updraft slopes slightly outwards with height. Indeed, the updraft locations given in Table 2 of EL77 are always inside of those calculated with the present model, except in the physically uninteresting $C = 0.2$, Ro < 10 cases.

To see why increasing drag coefficient displaces the maximum updraft inwards, consider solid body rotation given by $V = r\,\mathrm{Ro}\,f/2$ within the RMW, so that

$$\chi = r\,C\sqrt{\frac{f}{2K}}\,\frac{\mathrm{Ro}}{\sqrt{1+\mathrm{Ro}}} \qquad \textbf{(2.30)}$$

is proportional to r. Then the first term of w_∞ in (2.28) is proportional to r for small r, while the second behaves as r^2, so w_∞ is proportional to r at small radii. As $r \to \infty$, both terms tend to a constant limit. These changes in radial dependence are summarised in Table 2.1, and clearly are contained entirely within the expressions involving χ. Closer examination shows that w_∞ becomes close to constant once χ exceeds about 2. If χ is much less that this at the RMW, w_∞ will be close to proportional to r throughout the eye and the maximum updraft will lie near the RMW. As χ at the RMW increases, the large r limit begins to be felt and so w_∞ will increase less rapidly with radius. Once χ at the RMW reaches 2, the large r limit (i.e. that w_∞ is constant with radius) applies and so there is a noticeable inwards displacement and broadening of the maximum updraft. Even a very intense vortex with Ro = 100, $f = 3.8\times10^{-5}$ s^{-1}, $K = 20$ m^2 s^{-1}, $C = 0.005$ and $r =$ 30 km, gives only $\chi = 1.57$. However, EL77 allowed C up to 0.2, and found that the part of the eye over which w_∞ was proportional to r became smaller, and that the maximum updraft moved inwards, as C increased. In Fig 2.4, the values of χ at the RMW are 0, 0.27, 0.82 and 2.72, and only in the last does w_∞ become approximately constant with radius in the outer part of the eye, consistent with this analysis.

w_∞	$=$	$\frac{\chi+2}{2\chi^2+3\chi+2}$	$\frac{1}{r}\frac{\partial}{\partial r}\frac{rCV^2}{f+\zeta}$	$+$	$\frac{-2(\chi^2+4\chi+2)}{(2\chi^2+3\chi+2)^2}\frac{\partial\chi}{\partial r}$	$\frac{CV^2}{f+\zeta}$
Small r		~ 1	$\sim r$		~ -1	$\sim r^2$
Large r		$\sim r^{-1}$	$\sim r$		$\sim -r^{-2}$	$\sim r^2$

Table 2.1: Limiting behaviour of terms in (2.28) for small and large *r*, for the case of solid body rotation.

2.4 The boundary layer in a moving cyclone

Each of the azimuthal wave-number one components in the agradient flow in (2.19, 2.20) varies in height as an exponentially decaying sinusoid. The decay and oscillation depth scales δ_1 and δ_{-1} are respectively shorter and longer than the symmetric component's scale, δ_0. The phase of each component rotates with height. For (u_1, v_1), the imaginary parts of the coefficients of z and λ in the argument to the exponential function in (2.19) have opposite signs, so the phase rotates cyclonically with height. Similarly, from (2.20), the phase of (u_{-1}, v_{-1}) rotates anticyclonically where $I > V/r$, and cyclonically where $I < V/r$. The rate of rotation depends on the governing height scale, so it is always quicker for (u_1, v_1) than (u_{-1}, v_{-1}), and is also quicker in the inertially highly stable core of the cyclone. Approaching the limit $I = V/r$ from either side, the components become equal and constant with height, which corresponds to the double root $p_k = 0$. Physically, this is a surprising result, as it suggests that this component of the flow is not frictionally retarded. However, the other two components are retarded, and this component scales with the cyclone translation speed which was necessarily assumed to be much less than the gradient wind speed. Thus the absence of shear in this component is not unrealistic. A physical interpretation of the differing phase rotation with height and depth scales follows later.

Figure 2.5 shows the components of the asymmetric and total storm-relative flow at several heights, for the same cyclone as in Fig 2.2, but translating to the west at 5 m s^{-1}. Clearly (u_{-1}, v_{-1}) is several times stronger, and decays and rotates less rapidly with height, than (u_1, v_1). Inside the eye, where I is large and greater than V/r, both components have similar and relatively rapid rates of rotation with height, although in opposite directions.

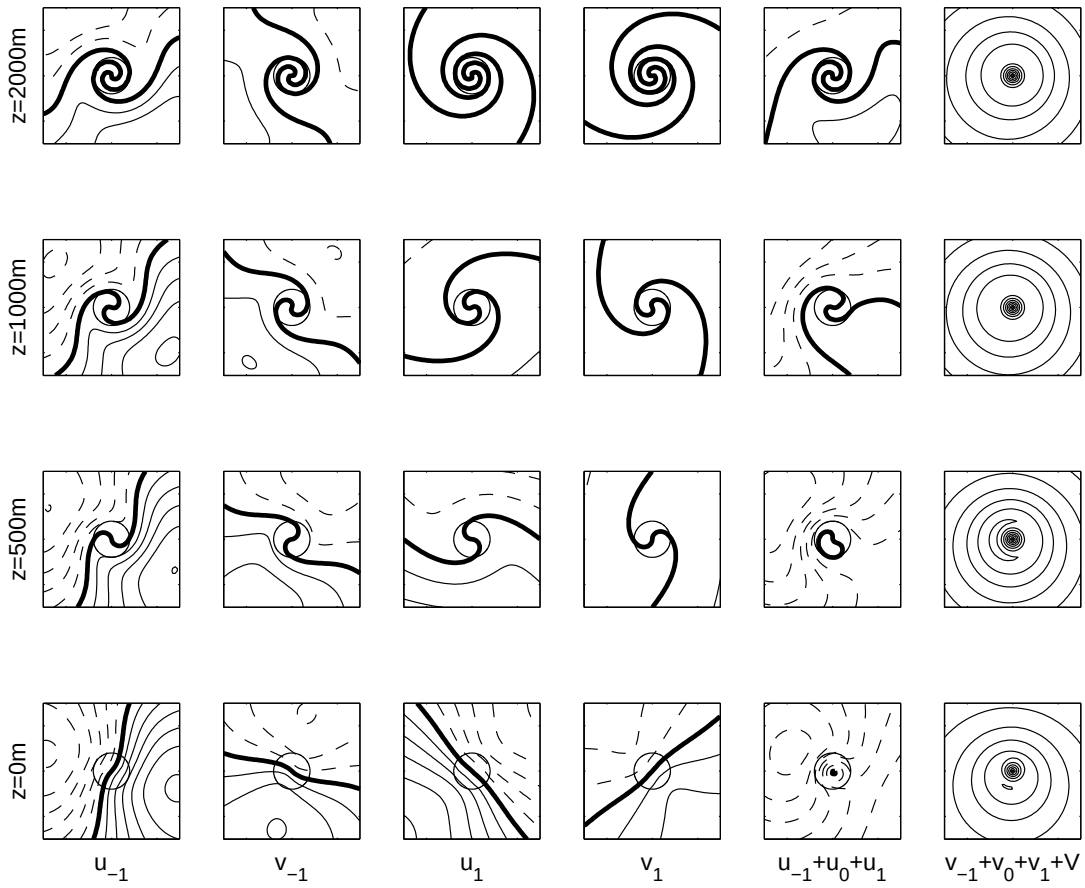

Figure 2.5: The two components of the asymmetric flow, (u_{-1}, v_{-1}) (left two columns) and (u_1, v_1) (middle two columns), together with the total storm-relative radial and azimuthal flow (last two columns) at the surface (bottom row), 500 m (second from bottom), 1 km (second top), and 2 km (top), for the cyclone in Fig 2.2, moving to the west at 5 m s^{-1}. The central circles in all except the last column show the RMW, and the domains are each 300 km square. The contour interval is 1 m s^{-1} in the first two columns, 0.25 m s^{-1} in the next two, 2 m s^{-1} in the fifth, and 5 m s^{-1} in the last. Negative contours are dashed, and the zero contour is bold.

The asymmetric part of the flow is dominated by (u_{-1}, v_{-1}), and consists of storm-relative inflow in the right forward quadrant and outflow in the left rear, in good agreement with observational studies (Shea and Gray 1973, Frank 1984). The slow anticyclonic rotation of this asymmetry with height is likewise consistent with Frank (1984, see Fig 1.6 here). Above 1 km in the right rear quadrant, the asymmetric outflow component u_{-1} dominates the symmetric inflow component u_0, due to its slower decay with height, giving a significant area of net outflow. This appears similar to the strong outflow found by Marks et al. (1999) in Hurricane Fran. Interestingly, there are two small regions near the surface where u_{-1} exceeds the translation speed U_t.

The asymmetry in the azimuthal flow gives a maximum on the left side near the surface in the total storm-relative flow, rotating towards the front with increasing height, due to the rotation with height of the dominant asymmetric term v_{-1}. The other term, v_1, makes a noticeable contribution only very near the surface. Again, this azimuthal flow is in reasonable agreement with the previously cited observational studies.

The effect of the asymmetries on the jet for the same storm are shown in the upper panels of Fig 2.6. The jet is strengthened in the left front quadrant where the asymmetric component v_{-1} is positive, and obliterated in the right rear. Here, the "jet factor" is defined as the ratio of the wind speed at the jet core to the gradient wind, in an earth-relative coordinate system. The asymmetry in height is less marked, particularly in the core when the jet is nearer the surface. This is because the bulk of the vertical variation in wind is explained by the symmetric part of the solution, with the asymmetric parts either being much weaker in the case of (u_1, v_1), or varying over a substantially longer depth scale in the case of (u_{-1}, v_{-1}). In either case, they produce weaker vertical shear than the symmetric component. Thus the height of the jet, where it exists, is not

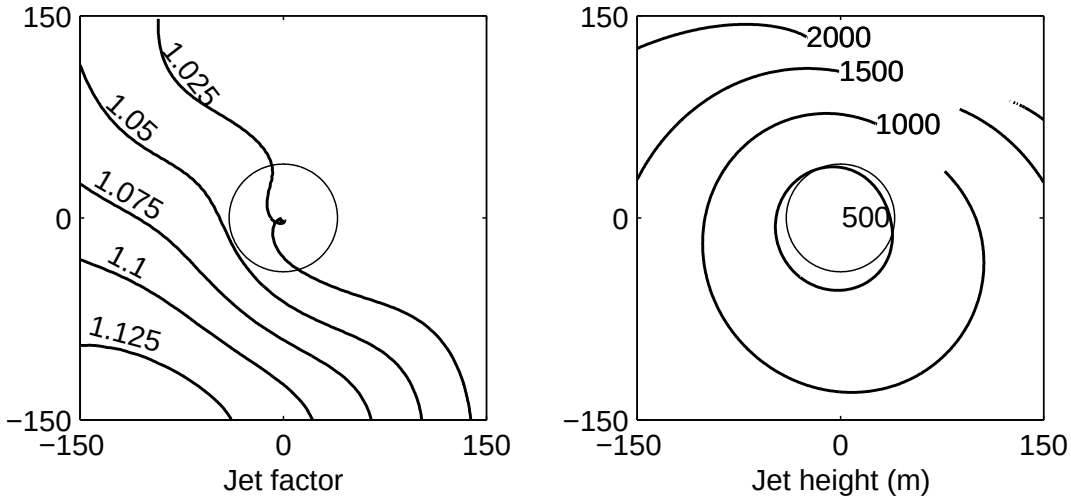

Figure 2.6: Jet strength, (left) and height (right), for the storm in Fig 2.5. Here, the jet strength is the ratio of the maximum earth-relative wind speed in the profile, to the gradient earth-relative wind speed. The central circles show the radius of maximum winds. Contours of jet height are discontinuous in the rear right quadrant of the storm, as there is no jet there.

dramatically modified from the symmetric case, although its strength is.

The effect of translation on the vertical velocity and surface wind factor are shown in Fig 2.7. Above the boundary layer, the wave number 1 asymmetry induces an enhanced updraft in the left forward quadrant, whilst eliminating the updraft at the right rear. The weak anticyclonic spiral in the updraft is a consequence of the dominant asymmetric (u_{-1}, v_{-1}) component. It is clearly not a forcing for spiral bands, but may be partly responsible for convective asymmetries in the eye-wall. There is a broad left-right gradient of the surface wind reduction factor (SWF), with relatively stronger surface winds on the weaker side of the storm, as well as the enhanced values near the centre noted earlier. The gradient is stronger when calculated with storm-relative winds than with earth-relative, but is present in both cases. This left-right asymmetry does not seem to have been previously noted, and is another possible dynamical explanation for the aforementioned variation in observed surface wind reduction factors.

2.4.1 Physical interpretation of the asymmetries

If the time derivative is restored and the friction terms removed from the original linear equations (2.2), the resulting system has an infinite family of inertia waves as solutions, given (to within arbitrary phase and amplitude) by

$$\begin{aligned} u(t,\lambda) &= \sqrt{\frac{f + 2V/r}{f + V/r + \partial V/\partial r}}\cos\left(\left(I + \frac{Vk}{r}\right)t - k\lambda\right) \\ v(t,\lambda) &= -\sin\left(\left(I + \frac{Vk}{r}\right)t - k\lambda\right) \end{aligned} \qquad \textbf{(2.31)}$$

For the case of interest $|k| = 1$, these have phase angular velocity $V/r \pm I$; that is, I in either direction, Doppler shifted by the cyclone's gradient flow. For the moment, these

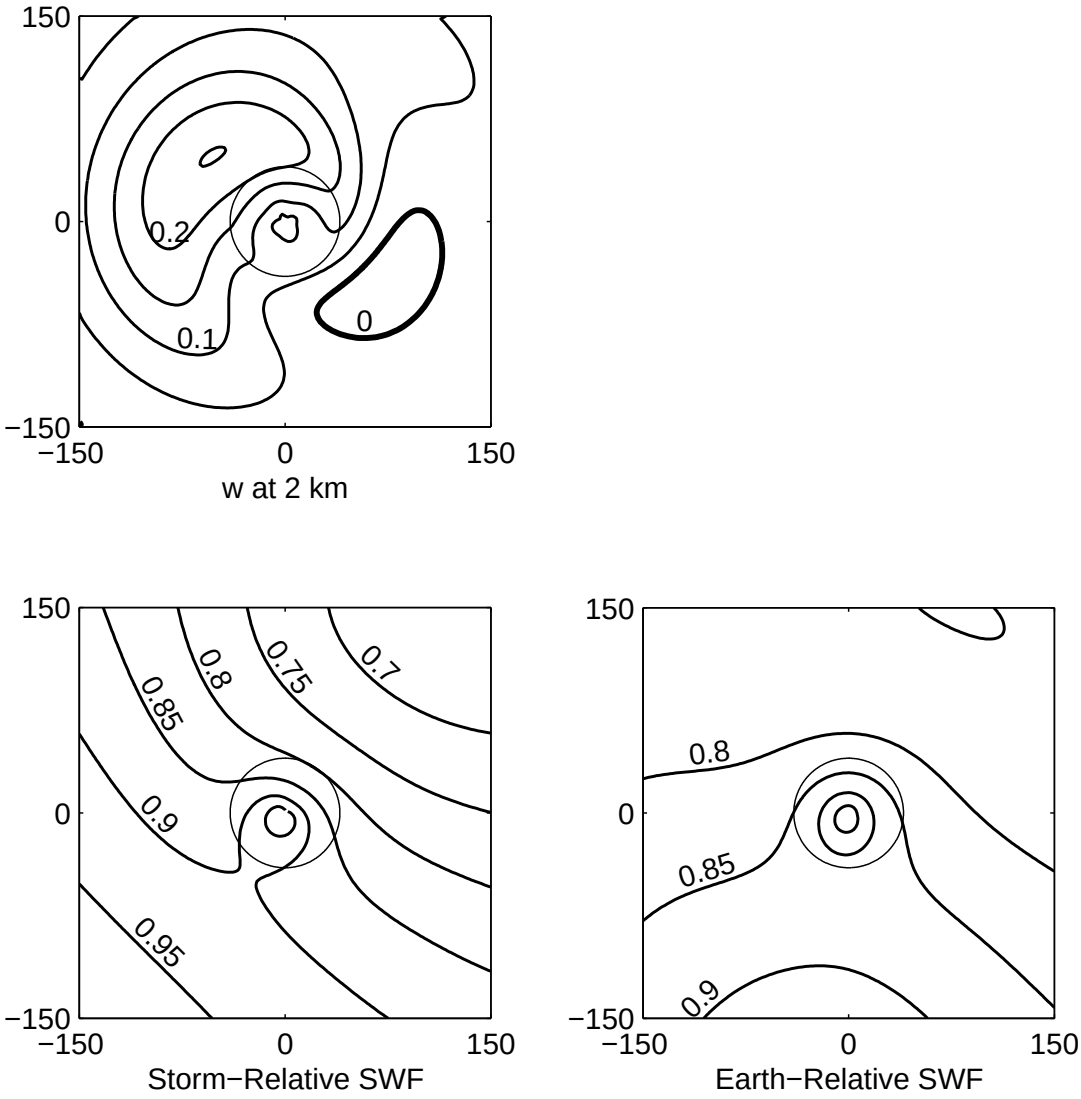

Figure 2.7: Top left: Vertical velocity at 2-km height for the same storm as in Fig 2.5. Lower left: Surface-wind reduction factor (SWF) using storm-relative winds; that is, the ratio of the storm-relative surface wind speed to the storm-relative gradient wind speed. Lower right: SWF for earth-relative winds. (Note that the similar figure showing the SWF in Kepert (2001) was incorrectly labelled as using earth-relative winds when it was in fact calculated from the storm-relative azimuthal components).

will be called the “fast” and “slow” waves, depending on whether they are propagating with or against the flow, respectively. The fast wave always travels cyclonically, while the slow wave will propagate anticyclonically in the inertially highly stable cyclone core, but may go the other way or be stationary in regions of weak inertial stability.

Although supported by the linearised inviscid equations of motion, the waves probably have little physical significance as they stand. For instance, their phase angular velocity is a strong function of radius, so the radial phase relationship will vary with time. Moreover, the wave (2.31) is divergent. The pattern of divergence will have a complex time evolution due to the radial variation of azimuthal velocity V, but the associated mass changes have been eliminated by the linearisation. The importance of these waves is rather that they provide a physical interpretation of the two asymmetric components. It will now be shown that in the viscid case, the vertical structure of these waves is such that friction brings them to a halt.

These waves have the same azimuthal structure as the solution components (u_1,v_1) and (u_{-1},v_{-1}). The friction $K\partial^2/\partial z^2$ term in those components is always in quadrature with the velocity field, and lagging, relative to the direction of propagation of the corresponding wave. Thus friction can only retard the waves, and not change their amplitude.

Moreover,

$$\begin{aligned} \frac{\text{amplitude } (u_1)}{K \text{ amplitude } (\partial^2 u_1/\partial z^2)} &= I + \frac{V}{r} \\ \frac{\text{amplitude } (u_{-1})}{K \text{ amplitude } (\partial^2 u_{-1}/\partial z^2)} &= \left| I - \frac{V}{r} \right| \end{aligned} \qquad \textbf{(2.32)}$$

and similar relationships apply for the v components. This, in combination with the quadrature phase relationship, shows that precisely enough friction is present to retard the wave to stationarity. In the case where $I = V/r$, the wave is already stationary, no retardation of the wave is required, and so no vertical shear is present in (u_{-1}, v_{-1}).

Now, (u_1, v_1) corresponds to the fast wave, and thus requires relatively more friction to stop it, than (u_{-1}, v_{-1}). Hence the former has a shorter vertical length scale, giving relatively stronger shear, than the latter. Moreover, since K is constant here, and the amplitude of each wave decreases with height, it is easy to see that the vertical stress divergence can only phase-lag the wave if the phase of the wave rotates in height in the same direction as it would have propagated in the absence of friction. Thus the phases of (u_1, v_1) and (u_{-1}, v_{-1}) will generally rotate in opposite directions, with height.

This physical interpretation can be extended to deduce the structure of the higher wave-numbers in (2.6). While these are not present in the current model, they could be excited by either nonlinear interaction of the wave-number one components, or by a surface boundary condition containing higher wave-number asymmetries because, for example, the cyclone was partly over land. For each pair of wave-numbers $\pm k$, the direction of the phase angular velocity $c_k = V/r + I/k$ of the inviscid wave determines the direction of rotation with height of the corresponding component of the solution to the viscid equations. Since $I < f + 2V/r$ in tropical cyclones[4], absolute wave-numbers three and higher can be expected to rotate cyclonically with height. For wave-number 2, the anticyclonically rotating component is possible only near and within the RMW, with the precise details depending on the Rossby number. The magnitude $|c_k|$ of the phase velocity is inversely related to the height scale, with (2.21) giving $\delta_k = (2K / k\,|c_k|)^{½}$.

[4]Except possibly for a small area within the RMW.

2.5 The impact of vertical advection on the jet strength

The hypothesis under consideration is that steady supergradient flow could exist in the boundary layer of a tropical cyclone only if there was a mechanism to force inflow in the presence of the jet against gradient adjustment, which would tend to destroy inflow. In the linear model, inflow is forced at the jet height by upwards turbulent transport of inflow from near the surface, and is sufficient to produce winds that were a few percent supergradient. The forcing of inflow by the updraft was calculated and found to be similar in magnitude to the turbulent forcing, so it was argued that the linear model significantly underestimates the jet strength. In this section, the linear model is extended to include a crude representation of vertical advection, and the salient properties of the extended model are outlined.

Restoring the vertical advection terms in (2.3) gives

$$2\gamma \frac{\partial \omega}{\partial \lambda} + \frac{w}{K} \frac{\partial \omega}{\partial z} + 2i \sqrt{\alpha\beta}\, \omega - \frac{\partial^2 \omega}{\partial z^2} = 0 \qquad \textbf{(2.33)}$$

where w is the vertical velocity and other variables are as before. It is not in general possible to solve this directly with w determined from u and v through the continuity equation, but it is straightforward if w is assumed to be constant with height. This will clearly be invalid near the surface, but is approximately true near the jet, in the upper boundary layer. Then, seeking as before solutions of the form

$$\omega(\lambda,z) = \sum_{k=-\infty}^{\infty} A_{kw} \exp(p_{kw} z + ik\lambda) \qquad \textbf{(2.34)}$$

for complex constants A_{kw}, gives equations for the p_{kw}:

$$-2i\,(k\gamma + \sqrt{\alpha\beta}) - \frac{w}{K}\,p_{kw} + p_{kw}^2 = 0 \qquad \textbf{(2.35)}$$

with solutions

$$p_{kw} = \frac{w}{2K} \pm \left(\sqrt{\sqrt{\left(\sqrt{\alpha\beta} + k\gamma\right)^2 + \frac{1}{4}\left(\frac{w}{2K}\right)^4} + \frac{1}{2}\left(\frac{w}{2K}\right)^2} + i\sqrt{\sqrt{\left(\sqrt{\alpha\beta} + k\gamma\right)^2 + \frac{1}{4}\left(\frac{w}{2K}\right)^4} - \frac{1}{2}\left(\frac{w}{2K}\right)^2} \right). \qquad \textbf{(2.36)}$$

Clearly taking the minus sign here will result in p_{kw} having a negative real part, necessary for the solution to decay with height. For simplicity, attention is restricted to the most important case $(\alpha\beta)^{1/2} + k\gamma > 0$, since the other cases are unlikely to be associated with large values of w. Before applying the surface boundary condition (2.12) to these, note that the decay and oscillation length scales of the solution are now different, because the real and imaginary parts of p_{kw} are unequal when $w \neq 0$. Indeed, in an updraft,

$$\begin{aligned}
|\mathrm{Im}(p_{kw})| &= \sqrt{\sqrt{\left(\sqrt{\alpha\beta} + k\gamma\right)^2 + \frac{1}{4}\left(\frac{w}{2K}\right)^4} - \frac{1}{2}\left(\frac{w}{2K}\right)^2} \\
&= \sqrt{\sqrt{\left(\sqrt{\alpha\beta} + k\gamma\right)^2 + \frac{1}{4}\left(\frac{w}{2K}\right)^4} - \frac{1}{2}\left(\frac{w}{2K}\right)^2} + \sqrt{\left(\frac{w}{2K}\right)^2} - \frac{w}{2K} \\
&\geq \sqrt{\sqrt{\left(\sqrt{\alpha\beta} + k\gamma\right)^2 + \frac{1}{4}\left(\frac{w}{2K}\right)^4} - \frac{1}{2}\left(\frac{w}{2K}\right)^2 + \left(\frac{w}{2K}\right)^2} - \frac{w}{2K} \qquad \textbf{(2.37)} \\
&= \sqrt{\sqrt{\left(\sqrt{\alpha\beta} + k\gamma\right)^2 + \frac{1}{4}\left(\frac{w}{2K}\right)^4} + \frac{1}{2}\left(\frac{w}{2K}\right)^2} - \frac{w}{2K} \\
&= |\mathrm{Re}(p_{kw})|
\end{aligned}$$

while in a downdraft

$$
\begin{aligned}
|\mathrm{Re}(p_{kw})| &= -\frac{w}{2K} + \sqrt{\sqrt{(\sqrt{\alpha\beta} + k\gamma)^2 + \frac{1}{4}\left(\frac{w}{2K}\right)^4} + \frac{1}{2}\left(\frac{w}{2K}\right)^2} \\
&\geq \sqrt{|\sqrt{\alpha\beta} + k\gamma|} \\
&= \delta_k^{-1}
\end{aligned}
\qquad \textbf{(2.38)}
$$

In either case,

$$
\begin{aligned}
|\mathrm{Im}(p_{kw})| &= \sqrt{\sqrt{\left(\sqrt{\alpha\beta} + k\gamma\right)^2 + \frac{1}{4}\left(\frac{w}{2K}\right)^4} - \frac{1}{2}\left(\frac{w}{2K}\right)^2} \\
&\leq \sqrt{\sqrt{\left(\sqrt{\alpha\beta} + k\gamma\right)^2} + \frac{1}{2}\left(\frac{w}{2K}\right)^2 - \frac{1}{2}\left(\frac{w}{2K}\right)^2} \\
&= \sqrt{\sqrt{\alpha\beta} + k\gamma} \\
&= \delta_k^{-1}
\end{aligned}
\qquad \textbf{(2.39)}
$$

Summarising,

$$
\begin{aligned}
&| \mathrm{Re}(p_{kw}) |^{-1} \geq | \mathrm{Im}(p_{kw}) |^{-1} \geq \delta_k && w \geq 0 \\
&| \mathrm{Im}(p_{kw}) |^{-1} \geq \delta_k \geq | \mathrm{Re}(p_{kw}) |^{-1} && w \leq 0
\end{aligned}
\qquad \textbf{(2.40)}
$$

with equality applying if and only if $w = 0$.

Thus, while the oscillation length scale $1/|\mathrm{Im}(p_{kw})|$ is always lengthened by vertical motion, the effect on the decay scale $1/|\mathrm{Re}(p_{kw})|$ depends on the sign of w. In an updraft, the slower decay of the spiral with height will lead to a higher, more strongly supergradient maximum in the upper boundary layer, than in the $w = 0$ case. Conversely, in a downdraft, the more rapid decay will result in a weaker (or absent) maximum at the top of the boundary layer. This applies to each of the three components of the solution.

Applying the slip boundary condition (2.12) yields

$$A_{0w} = -\frac{\chi_+\left(\frac{\chi_+}{\chi_-} + i\left(1 + \chi_+\left(1 - \frac{w_*}{2}\right)\right)\right) V}{2 + \chi_+(3 - w_*) + \chi_+^2\left(2 - \frac{3w_*}{2}\right)} \tag{2.41}$$

$$\begin{aligned} A_{1w} = {} & -\eta_+\left[\left(\sqrt{\beta/\alpha} - 2\right)\left(1 - w_*\psi_+/2 - i\psi_+/\psi_-\right) + 2\psi_+\left(\sqrt{\beta/\alpha} - 1\right)\right] U_t \\ & \div \left[\, 2\left(1 + i\eta_+/\eta_-\right)\left(1 - i\psi_+/\psi_-\right) \right. \\ & + \left(3 - w_*\right)\left(\eta_+(1 - i\psi_+/\psi_-) + \psi_+(1 + i\eta_+/\eta_-)\right) \\ & \left. + \eta_+\psi_+\left(4 - 3w_* + w_*^2/2\right) \,\right] \end{aligned} \tag{2.42}$$

and

$$\begin{aligned} A_{-1w} = {} & -\psi_+\left[\left(\sqrt{\beta/\alpha} + 2\right)\left(1 - w_*\eta_+/2 - i\eta_+/\eta_-\right) + 2\eta_+\left(\sqrt{\beta/\alpha} - 1\right)\right] U_t \\ & \div \left[\, 2\left(1 - i\eta_+/\eta_-\right)\left(1 + i\psi_+/\psi_-\right) \right. \\ & + \left(3 - w_*\right)\left(\eta_+(1 + i\psi_+/\psi_-) + \psi_+(1 - i\eta_+/\eta_-)\right) \\ & \left. + \eta_+\psi_+\left(4 - 3w_* + w_*^2/2\right) \,\right] \end{aligned} \tag{2.43}$$

where

$$\begin{aligned} \chi_+ &= \frac{CV}{K\sqrt{\sqrt{\alpha\beta + \frac{1}{4}\left(\frac{w}{2K}\right)^4} + \frac{1}{2}\left(\frac{w}{2K}\right)^2}} \\ \chi_- &= \frac{CV}{K\sqrt{\sqrt{\alpha\beta + \frac{1}{4}\left(\frac{w}{2K}\right)^4} - \frac{1}{2}\left(\frac{w}{2K}\right)^2}} \end{aligned} \tag{2.44}$$

$$\eta_+ = \frac{CV}{K\sqrt{\sqrt{(\sqrt{\alpha\beta}+\gamma)^2+\frac{1}{4}\left(\frac{w}{2K}\right)^4}+\frac{1}{2}\left(\frac{w}{2K}\right)^2}}$$

$$\eta_- = \frac{CV}{K\sqrt{\sqrt{(\sqrt{\alpha\beta}+\gamma)^2+\frac{1}{4}\left(\frac{w}{2K}\right)^4}-\frac{1}{2}\left(\frac{w}{2K}\right)^2}} \qquad \textbf{(2.45)}$$

$$\psi_+ = \frac{CV}{K\sqrt{\sqrt{(\sqrt{\alpha\beta}-\gamma)^2+\frac{1}{4}\left(\frac{w}{2K}\right)^4}+\frac{1}{2}\left(\frac{w}{2K}\right)^2}}$$

$$\psi_- = \frac{CV}{K\sqrt{\sqrt{(\sqrt{\alpha\beta}-\gamma)^2+\frac{1}{4}\left(\frac{w}{2K}\right)^4}-\frac{1}{2}\left(\frac{w}{2K}\right)^2}} \qquad \textbf{(2.46)}$$

and

$$w_* = \frac{w}{CV} \qquad \textbf{(2.47)}$$

These reduce to (2.14, 2.15) when $w = 0$.

Figure 2.8 gives examples of profiles in a symmetric stationary storm for positive, zero and negative *w*. The features discussed above are apparent, in that the wind speed maximum is raised and strengthened by the updraft, and practically eliminated in the downdraft. Mathematically, this results from the inequality of the decay and oscillation scales. However, this is also physically consistent with the earlier discussion, in that the updraft cases have stronger inflow and greater angular momentum advection in the lower part of the supergradient layer. Moreover, the steeper gradient $\partial u/\partial z$ in the updraft

cases will provide stronger forcing of inflow by vertical advection and diffusion there. Note also that the layer of outflow above the jet, which results from an adjustment back to gradient balance of the supergradient flow diffused and advected upwards, is stronger when an updraft is present. Conversely, the jet and outflow layer are weakened (or nonexistent) and lower in a downdraft.

The continuity equation was not used in deriving these profiles – indeed, it is violated because the vertical motion is constant with height. Moreover, this approximation would be expected to produce its largest errors near the surface. However, the stronger near-surface inflow in the updraft cases will tend to be associated with increased surface convergence there. Thus this solution is broadly consistent with continuity.

It is thus reasonable to speculate that there is a positive feedback mechanism, where an updraft results in stronger surface inflow and enhanced surface convergence, thereby reinforcing the updraft through continuity. This may be of importance in the dynamics of rain-bands. Several studies have investigated the dynamics of waves on a tropical-cyclone like basic state. For example, Willoughby (1977, 1978) showed spiral rain-bands had features in common with inwardly propagating inertia-buoyancy waves. Conversely, Guinn and Schubert (1993) have argued that vortex Rossby waves provide an explanation of the observed structure of inner bands, and that outer bands are formed through the stretching out of potential vorticity anomalies . However, these studies have not included a boundary layer, and thus this possible effect has been neglected.

In summary, the inclusion of vertical advection – albeit not in a physically realistic form – results in a higher, stronger jet in an updraft, and a weaker or absent jet

in a downdraft. Moreover, there is an increased lower boundary-layer inflow associated with the updraft which may be part of a positive feedback mechanism relevant to the dynamics of rainbands. However, these results should be regarded as indicative only, due to the unrealistic vertical velocity profile prescribed here. The numerical solution of the full equations of motion, to be considered in the next chapter, will allow a more realistic treatment of the effects of vertical advection.

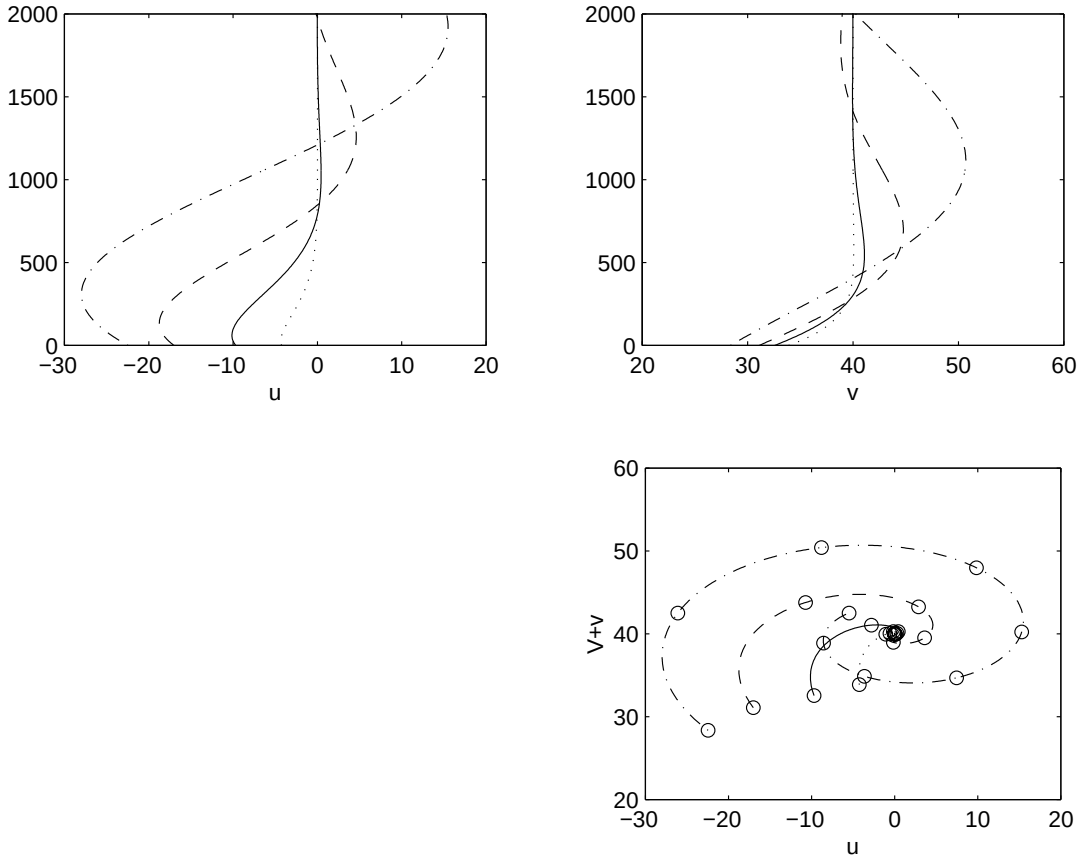

Figure 2.8 Profiles of radial (left top) and azimuthal (right top) flow, together with a hodograph (bottom) in a symmetric cyclone according to (2.33, 2.38), for $w = 0.5$ m s^{-1} (dash-dotted), $w = 0.25$ m s^{-1} (dashed), $w = 0$ (solid) and $w = -0.25$ m s^{-1} (dotted). Other parameters are $V = 40$ m s^{-1}, $r = 40$ km, $f = 3.77 \times 10^{-5}$ s^{-1}, $C = 0.002$ and $K = 50$ m^2 s^{-1}. The circles on the hodographs are every 500 m of height.

2.6 Concluding Remarks

The properties of a supergradient low-level jet have been examined using a linear analytical model of the tropical cyclone boundary layer, which also enabled deductions as to the driving mechanisms. This model diagnoses the boundary-layer flow as the frictional response to an imposed, prescribed gradient flow characteristic of a cyclone, but ignores the feedback from boundary-layer processes onto the cyclone as a whole. The solution bears some resemblance to the well-known Ekman boundary-layer model. However, it has three component: a symmetric one due to the cyclone, and two asymmetric ones resulting from the interaction of the moving cyclone with the underlying surface. Each has a different depth scale, which vary from that of the classical Ekman solution. There is also an asymmetry between the radial and azimuthal components of the flow not present in the classic solution, which makes the radial component relatively stronger than the azimuthal in all three components. The symmetric component is an improvement of the symmetric vortex models of Rosenthal (1962) and EL77, while the asymmetric solution is believed to be new.

It was shown that strong inwards advection of absolute angular momentum was necessary to produce the jet. In the linear model, the required inflow was maintained against gradient adjustment by vertical diffusion, and the wind maximum was found to be a few percent supergradient in a stationary cyclone. It was argued that vertical advection should be of similar size, and further strengthen the supergradient jet. It was speculated that the outer side of a rainband may be a preferred location for jet formation, since here there is stronger inflow and angular momentum gradient, and a stronger updraft.

The jet height was predicted to scale as $\delta_0 = (2K/I)^{1/2}$. It was argued that the

introduction of vertical advection to the linear model would not bring any new height scales but modify those already applying, and so this should also apply approximately in a full nonlinear model. It was shown using a crude representation of the vertical advection that the oscillation scale was always increased, while the decay length scale increased in an updraft and decreased in a downdraft. This confirms the above argument, and suggests that a stronger jet would be expected in regions of significant upward motion.

The Ekman spiral, at least in its original form, is nowadays generally regarded as a fairly poor model of the atmospheric boundary layer, yet here a related model is advanced as being appropriate in tropical cyclones. However, several of the factors which commonly disturb the classical Ekman spiral will apply to a much lesser degree in the tropical cyclone boundary layer, and so the model is not thereby invalidated. The first of these factors, the nonslip boundary condition, is here replaced by one of several possible slip conditions.

Second is the role of buoyancy in generating turbulence. In the strongly sheared environment of the tropical cyclone boundary layer, turbulence would be expected to be dominantly shear-generated. This would lead to a relatively simple turbulent diffusivity structure, not subject to large diurnal variations. In the normal atmospheric boundary layer, the time scale $1/f$ for the establishment of an Ekman spiral is similar to the time over which diurnally induced variations in diffusivity occur. Hence it is perhaps hardly surprising that it is rarely observed over the land. Indeed, it is worth noting that Taylor (1915), in his comparison of aircraft data to an Ekman spiral (with a slip boundary condition), restricted attention to the strong wind case for precisely this reason. In a tropical cyclone, on the other hand, significant diurnal changes in turbulent diffusivity

do not occur, and the time scale $1/I$ for boundary-layer adjustment is much shorter, so the boundary-layer winds are much more likely to be in equilibrium with the diffusivity.

Another factor that can eliminate or even reverse the turning of the winds in the boundary layer is baroclinicity. This would be less important in a tropical cyclone, as the near-surface temperature gradients are weak (except near the eye) and tend to be aligned perpendicular to the flow. Near the eye, the thermal shear will tend to be directed against the gradient wind, and this will tend to sharpen the maximum in the upper boundary layer. Moreover, the altered scaling which results in a markedly shallower boundary layer here also reduces the extent to which temperature gradients can contribute to significant wind change across the boundary layer.

A final factor which, in contrast to the others, does apply in the tropical cyclone boundary layer, is the hydrodynamic instability of the Ekman spiral. For instance, the numerical studies of Faller and Kaylor (1966) and Lilly (1966), and the analytical work of Brown (1970, 1972a, 1972b), show that the classical Ekman spiral is unstable and breaks down into longitudinal rolls, aligned at approximately 14^{o} to 17^{o} to the geostrophic flow. Longitudinal rolls are well known to occur in the atmospheric boundary layer, and recently some evidence of their occurrence in the tropical cyclone boundary layer has appeared (Wurman and Winslow, 1998).

Is the jet, then, nothing more than the weakly supergradient flow found near the top of the Ekman boundary layer? In the context of the linear model, the answer is essentially yes; albeit with the complication of three separate components in a moving storm. However, it was indicated here, and will be confirmed in Chapter 3 using a numerical model, that vertical advection plays a crucial role in strengthening the jet, and

that the supergradient component may be several times stronger than is predicted by the linear model. The major role of upwards advection seems to be peculiar to intense vortices and does not occur in more normally considered cases. This is because the rapid, almost step-like increase in inertial stability near the radius of maximum winds produces an updraft which is much stronger than would be expected from the classical theory, in which the updraft is proportional to the curl of the surface stress.

It was also shown that the distribution of vertical velocity outside the core region may not follow the predictions of the classical Ekman theory, as surface divergence may prevail even in the presence of cyclonic relative vorticity, provided the inertial stability is weak. Within the eye, the updraft is proportional to radius, in agreement with the results of Eliassen (1971) and EL77.

For a moving storm, it was found that the supergradient jet was generally located in the left forward quadrant of the storm (in the Northern Hemisphere), away from the strongest (earth-relative) near-surface winds in the right forward quadrant. The jet was substantially more supergradient than in the stationary case. The majority of the asymmetric flow was shown to be contained in the deeper of the two asymmetric components, with the shallower one being much weaker. The asymmetric components were interpreted as frictionally stalled inertia waves, where the decay and rotation depth scales adjust so as to provide precisely enough retardation to bring the wave to a halt. The asymmetric components introduce a wave number one asymmetry to the vertical motion, which is superimposed on that due to the symmetric component. The updraft is greatly strengthened in the right forward quadrant, while weak subsidence occurs to the left rear, in the Northern Hemisphere. This may contribute to the observed convective asymmetries in the tropical cyclone eye wall.

The ratio of the surface wind speed to the gradient wind speed is a useful parameter which has been widely studied. The linear model predicts that in a stationary storm, this will increase from approximately 0.7 at large radii, to 0.9 or more at and inside of the RMW. A similar trend is found in the observational analysis of Mitsuta et al. (1988). For a moving storm, there is additionally a left-to-right gradient, with higher values on the left side of the storm (Northern Hemisphere); that is, the side with the weaker surface winds. The use of a universal constant for surface wind reduction is thus not supported by the linear model. As discussed in the first chapter, observational studies have found wide variation in the surface wind factor, from approximately 0.55 to 1. While some of this variation can be ascribed to stability variations, these are not present here. Thus these dynamical factors appear to be a further cause of the observed variability.